Dynamics of the Caltech SSPP deployable structures: structure–mechanism interaction and deployment envelope

Narravula Harshavardhan Reddy* and Sergio Pellegrino†
California Institute of Technology, Pasadena, CA, 91125

The Caltech Space Solar Power Project has been developing ultralight deployable space structures consisting of thin-shell composite strips that support photovoltaic and RF elements. These modular, square structures can potentially be scaled to tens of meters in size. This paper studies the interaction between the deployment dynamics of the structure and the deployment mechanism, both experimentally and numerically. Instead of considering a full structure, a quadrant is considered to reduce the number of components and to better focus on the main parameters that affect the deployment behavior. Outcomes of this research will not only benefit the Caltech project but will also contribute to the design of future lightweight deployable space structures that undergo unconstrained dynamic deployment.

Nomenclature

$\mathbf{A}$	=	in-plane stiffness matrix
$\mathbf{D}$	=	out-of-plane stiffness matrix
d	=	radial position of CG of cylinder with respect to hinge axis
F	=	deploying force on the composite structure
F_{n1}, F_{n2}	=	total radial forces on pulleys
g	=	acceleration due to gravity
H	=	height of the center of strip from the position of the cords
h	=	vertical displacement of weights
I	=	rotation moment of inertia of pulley
I_h	=	rotation moment of inertia of deploying cylinder about hinge axis
$\mathbf{M}$	=	out-of-plane moments per length
M	=	mass of deploying cylinder
M_1, M_2	=	masses connected by cord over two pulleys
M_{f1}, M_{f2}	=	friction moments in pulleys
$\mathbf{N}$	=	in-plane forces per length
R	=	radius of pulley
r	=	inner radius of ball bearing
T_1, T_2, T	=	tensions in cord over two pulleys
T_e	=	moment due to elastic torsion spring
T_f	=	opposing moment due to friction in hinge
x, y, z	=	Cartesian coordinates
β	=	rotation of pulleys
ϵ	=	mid-plane strain
κ	=	mid-plane curvature
μ_1, μ_2	=	coefficients of friction relating moments and total radial forces
θ	=	angle of rotation of deploying cylinder
θ_0	=	angular position of CG of cylinder with respect to hinge axis

*Graduate Student, Graduate Aerospace Laboratories, MC 105-50. AIAA Student Member

†Joyce and Kent Kresa Professor of Aerospace and Civil Engineering; Jet Propulsion Laboratory Senior Research Scientist; Co-Director, Space-Based Solar Power Project, Graduate Aerospace Laboratories, MC 105-50. AIAA Fellow. E-mail: sergiop@caltech.edu

I. Introduction

Unconstrained dynamic deployment is driven by the release of the strain energy stored in a folded or coiled structure. While the structure is simply released and allowed to deploy on its own, the deployment can be guided by pulling the structure outward at specific points. Unconstrained deployment is less common in existing deployable structures, however, it can potentially lead to simpler and lighter mechanical components, and thus allows for lighter and more efficient deployable spacecraft. Studies of the fundamentals of uncontrolled deployment are relatively rare and in this paper we attempt to fill this gap by studying the deployment of the ultralight deployable space structures developed by the Caltech Space Solar Power Project (SSPP).

Figure 1 shows schematically the modular structural architecture adopted by the Caltech Space Solar Power Project. It consists of bending-stiff trapezoidal strips bounded by foldable longerons with a TRAC cross-section [1] that are connected by battens. The strips form structurally independent modules and are attached to diagonal cords suspended between the tips of four diagonal booms and a central mechanism. Of the four identical quadrants in the full architecture, the present study focuses on a single quadrant.

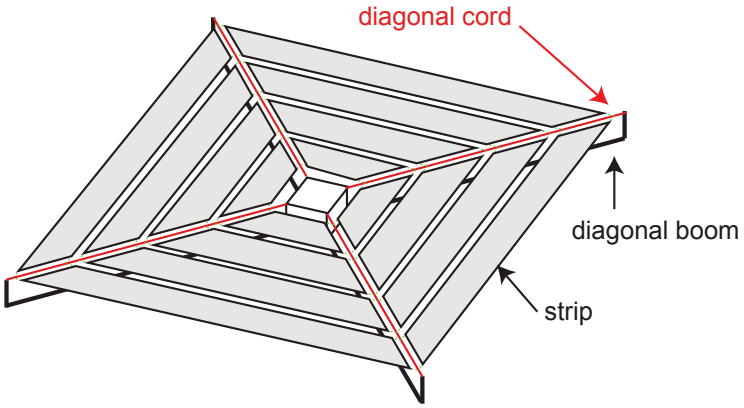

Fig. 1 Full architecture of the Caltech SSPP.

In particular, we are interested in studying how the motion of the structure during deployment is affected by the presence of the deployment mechanism, and by the rate at which the outer ends of the cords are pulled outwards during deployment. Metrics of interest are the time to fully deploy and the transverse motion of the structure during deployment, which is linked to its deployment envelope. This latter metric is important as it indicates whether the deploying structure clears any obstacles for a successful deployment that avoids damage or snagging against other components. Hence, in this study, we use the extreme heights (normal to the plane of the fully deployed structure) reached by the structure during deployment as a key metric.

The composite structure deploys dynamically due to its own stored strain energy. The deployment mechanism is designed to hold the structure in its folded configuration, to avoid premature deployment. Structural stability after the structure is fully deployed is provided by the diagonal cords, which are held under tension by the diagonal booms. Various components (such as the cords, deploying cylinder, pulleys) of the mechanism have an influence on the deployment dynamics. Two major factors affecting the deployment dynamics are as follows.

1) The deploying cylinder assists in maintaining a safe radius of curvature in the elastic folds and keeps the structure from deploying in stowed configuration. Once released, the cylinder rotates about the hinge axis and remains in contact with the structure for a significant duration thus imposing kinematic constraints on the structure.
2) The suspension cords carry the deploying force and dictate the speed of deployment. Since the three strips are assembled using the cords, the cords also impose kinematic constraints on the structure.

In this study, we investigate these two factors using experiments and finite element simulations.

II. Experimental setup

The only way to truly verify the fidelity of numerical simulations is to compare them with experiments. The composite structure of interest and the deployment mechanism that was designed to study its deployment are described below.

A. Structure

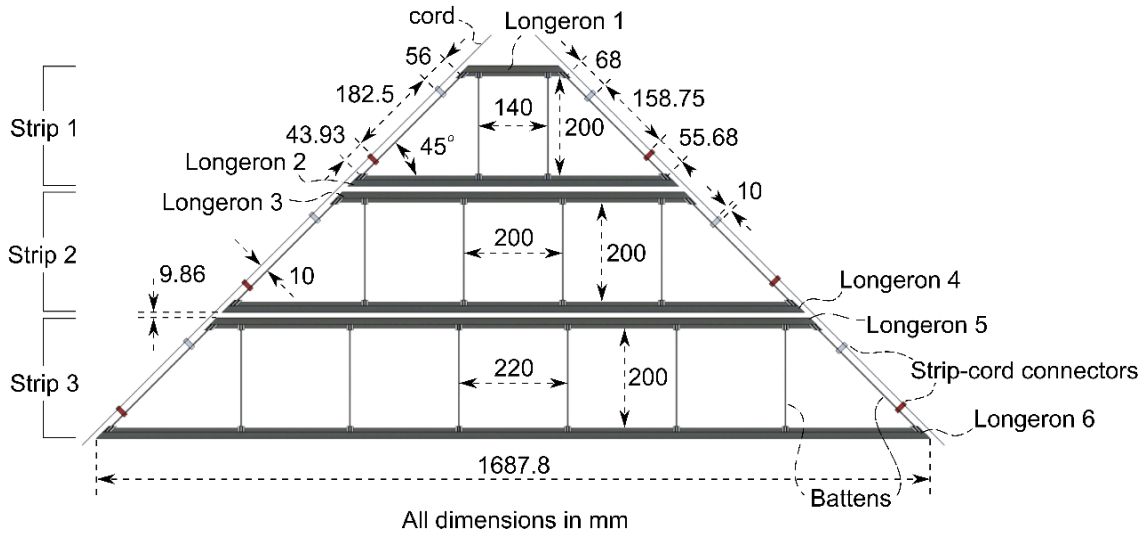

Fig. 2 Geometry of structure.

The composite structure used in this study comprises three strips (Figure 2). Each strip consists of two bending-stiff longerons of TRAC cross-section ([1, 2]) and have the composite layup shown in Figure 3. The composite layup in the flanges of a longeron is $[\pm 45_{GFPW}/0_{CF}/\pm 45_{GFPW}]$, and that in the web region is $[\pm 45_{GFPW}/0_{CF}/\pm 45_{3,GFPW}/0_{CF}/\pm 45_{GFPW}]$, where CF represents a thin ply with unidirectional Pyrofil MR 70 12P Carbon fibers made by Mitsubishi Chemical (30 gsm). GFPW represents plain weave scrim glass (25 gsm). Both plies are impregnated with North Thin Ply Technology's ThinPreg 415 resin. The longerons are fabricated in-house using the techniques laid out in [3]. A strip is made torsion-stiff by connecting its two longerons at specific locations by carbon fiber rods called battens. The battens, made of carbon fibers, have a rectangular cross-section with a width of 3 mm and thickness 0.6 mm. Placement of the battens in a strip and the placement of strips in relation to one another was adopted from [5]. The battens are bonded to the web regions of the longerons with epoxy.

The three strips are connected via cords. To support a strip with the cord, two 3D printed sleeves called strip-cord connectors are rigidly bonded to the leftmost and rightmost battens (Figure 2). The cord is bonded, using epoxy, to the outermost strip-cord connectors of every strip. These connectors are labeled as C12, C14, C16, C22, C24, and C26 in Figure 6.

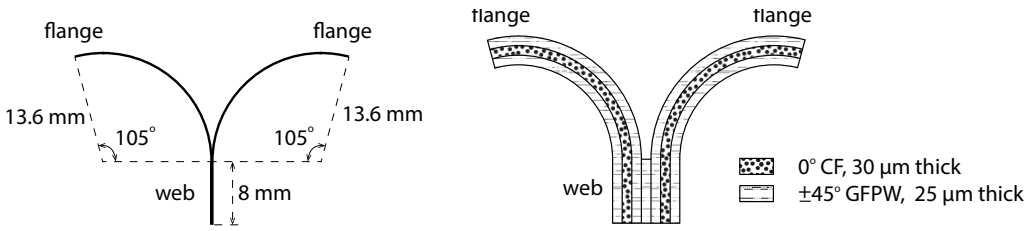

Fig. 3 Cross-section of a TRAC longeron. Each flange has the composition $[\pm 45_{GFPW}/0_{CF}/\pm 45_{GFPW}]$ and the web $[\pm 45_{GFPW}/0_{CF}/\pm 45_{3,GFPW}/0_{CF}/\pm 45_{GFPW}]$.

B. The deployment mechanism

Inspired by the designs described in [4, 5], we designed a simplified deployment mechanism that incorporates only the essential components (Fig. 5) to trigger the release of the structure and study its deployment, but does not provide other key functions of the full flight mechanism. Also, instead of using constant-force retractors attached to the ends of the diagonal cords, for the purpose of verifying the numerical simulations, hanging masses were used in our

Table 1 Mass properties of the composite structure.

Areal density of flange	1.196×10^{-4} g/mm^2
Areal density of web	2.908×10^{-4} g/mm^2
Density of batten	1.61×10^{-3} g/mm^3
Total mass of 6 longerons	45.4 g
Total mass of 18 battens	12.4 g
Total mass of 12 strip-cord connectors	7.5 g

experiments. The masses can be more easily tailored in the experiment, and are easier to quantify compared to other sources of deployment force such as retractor springs.

The deployment mechanism shown in Figure 4 is built around a rigid cylinder labelled central shaft. Two annular plates made of acrylic are placed at the top and bottom of this shaft to mimic the mechanism in [4, 5]. The central shaft supports the quick release mechanism at the very top and is connected to the hinge and diagonal frames at the bottom. One end of each of the two cords is rigidly attached to the central shaft. The metallic frames placed along the diagonals of the quadrant support pulleys mounted on vertical columns at the outer ends. The central shaft, deploying cylinder, and the hinge components are made of aluminum while the top and bottom plates are made of acrylic.

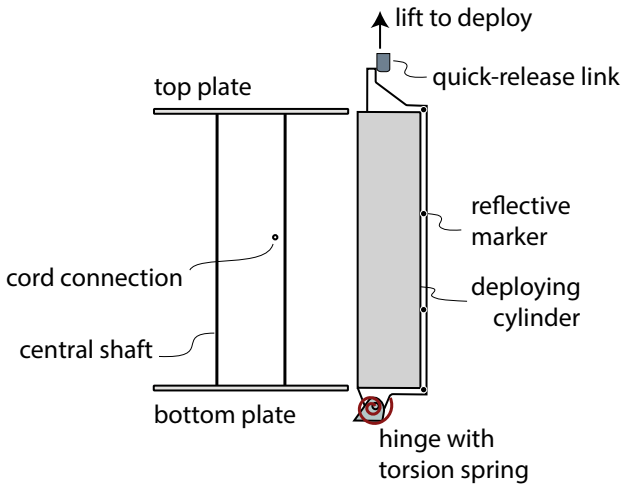

Fig. 4 Schematic of the deployment mechanism in stowed configuration. The middle portion of the folded structure lies in between the central shaft and deploying cylinder. One end of each cord is attached to the central shaft at the cord connection point.

C. Motion capture

In order to verify the numerical simulations of the deployment, the motion of the structure was recorded using six infrared motion capture cameras, set a frame rate of 180 fps, marketed as *Prime 41* by *NaturalPoint Inc*. These cameras track the reflective markers attached to the structure at chosen locations. Flat reflective stickers were attached at all the longeron-batten intersections. A reflective sticker was placed also on the webs of the longerons, in the middle of two longeron-batten intersections. These flat markers are shown as white dots in Figure 6. In addition, to track the motion of the strip-cord connectors, reflective spheres 6.4 mm in diameter were glued to the connectors.

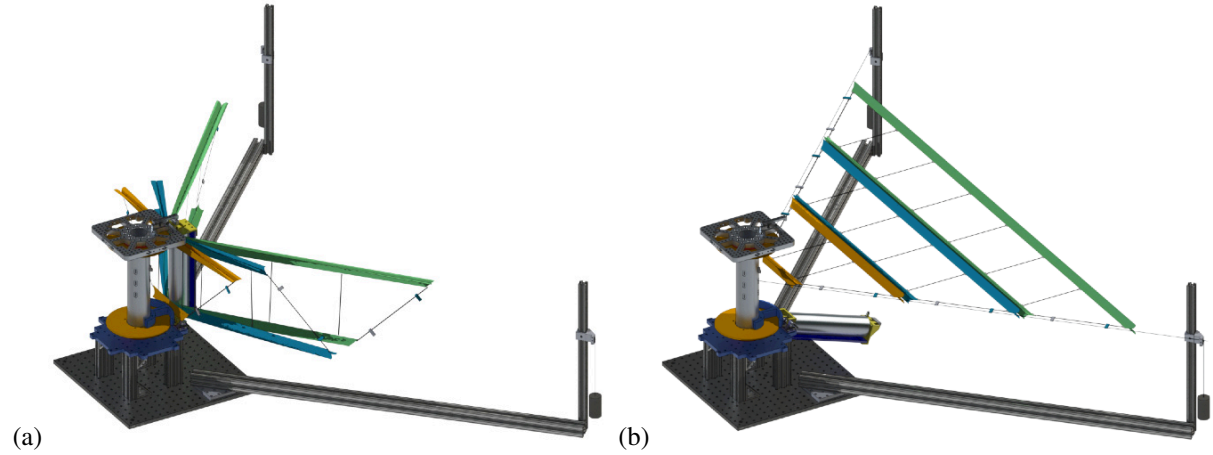

Fig. 5 Deployment mechanism and structure in (a) stowed and (b) deployed configurations. Strip 1 of the structure is shown in orange, Strip 2 in blue, and Strip 3 in green.

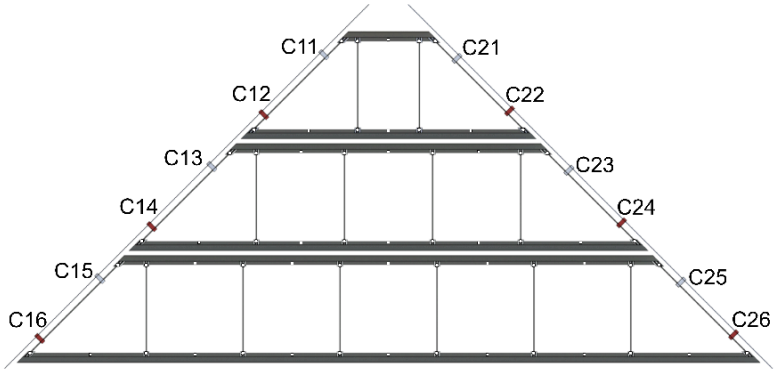

Fig. 6 Reflective stickers are glued to the structure at the intersections of longerons and battens, and on the web regions of the TRAC longerons between in between battens. Reflective spheres attached to strip-cord connectors are labeled *C*.

III. Characterization of composite laminates and deployment mechanism

To develop high-fidelity simulations of the dynamic deployment, it is essential to quantify the constitutive behavior of the composites, tensile behavior of the cords, and friction in the hinge and pulleys (shown in Fig. 5). The quantities measured will be used in the dynamic simulations presented in Section IV.

A. Material properties

The elastic stiffness of the flange and web laminates (Figure 3) was modeled with the generalized stiffness matrices $\boldsymbol{A}, \boldsymbol{D}$ for symmetric laminates [6],

$$\begin{Bmatrix} \boldsymbol{N} \\ \boldsymbol{M} \end{Bmatrix} = \begin{bmatrix} \boldsymbol{A} & \boldsymbol{0} \\ \boldsymbol{0} & \boldsymbol{D} \end{bmatrix} \begin{Bmatrix} \boldsymbol{\epsilon} \\ \boldsymbol{\kappa} \end{Bmatrix}, \tag{1}$$

where $\boldsymbol{N}$ and $\boldsymbol{M}$ are the in-plane forces and out-of-plane moments per unit length, $\boldsymbol{\epsilon}$ and $\boldsymbol{\kappa}$ are the mid-plane strains and curvatures, respectively; $\boldsymbol{A}$ is the in-plane stiffness matrix, and $\boldsymbol{D}$ is the bending stiffness matrix.

To fold a longeron, the flanges are first flattened inducing a bending strain in the transverse direction (along the circumference of the circular arc, direction 2) followed by bending the flanges and web in longitudinal direction (direction 1). Hence, the elements of the stiffness matrices $\boldsymbol{D}$ contributing significantly to the stored strain energy due to bending are D_{11}^{web}, D_{11}^{flange} and D_{22}^{flange}.

We conducted four-point bending tests on the flange and web laminates to experimentally measure the stiffness values D_{11} and D_{22}, and tensile tests in longitudinal direction to measure the compliance values a_{11} and a_{21}, where the compliance matrix $\boldsymbol{a} = \boldsymbol{A}^{-1}$. The missing elements of $\boldsymbol{D}$ and $\boldsymbol{a}$ for both flange and web laminates were taken from an earlier study [3] conducted on similar laminates. The non-zero stiffness values used in the numerical simulations are listed in Table 2.

Table 2 Generalized stiffness values for flange and web laminates.

	A_{11} (N/mm)	A_{12} (N/mm)	A_{22} (N/mm)	A_{33} (N/mm)	D_{11} (Nmm)	D_{12} (Nmm)	D_{22} (Nmm)	D_{33} (Nmm)
Flange	6218.5	637.38	1078.55	736.5	0.76	0.48	0.59	0.46
Web	11476.1	1112.8	2291.54	1727.4	39.61	4.32	10.42	4.93

B. Behavior of the cord

Cords are the primary members carrying the deploying force in addition to holding various strips of the structure together (Figures 2 and 5). Knowing the tensile behavior of the cord helps accurately estimate the transfer of forces along the cord in numerical simulations. In addition, deformed lengths of the various segments of a cord decide the positions of the strips relative to one another (see Figure 14).

Cords used in this study are 8 strand weave fishing lines with a load rating of 50 lb, marketed as J-Braid by Daiwa. To measure the elastic behavior (reaction force vs extension) of these cords, we conducted tensile tests on a sample using Instron machine. Extension was measured using two laser extensometers (LE-01 and LE-05 from Electronics Instrument Research), and the reaction force in the cord was measured using a 500 N load cell. The resulting data (Figure 7) was given as a direct input (in the form of a table) to the simulations.

C. Characterization of the hinge

Deployment of the structure begins the instant the deploying cylinder is released. Initial dynamics of the structure depends on the rotational speed of the cylinder. This speed in turn is governed by the stiffness of the torsion springs and friction in the hinge (see Figure 4). Therefore, quantifying the elastic and friction contributions to the moment at the hinge axis is essential to accurately simulate the initial dynamics of the deployment. Elastic stiffness of the torsion springs was obtained from the data sheets, and was verified experimentally. To measure the friction moment at the hinge axis, we released only the cylinder, without any structure, and tracked its motion using motion capture cameras (Figure 4). The measured rotation of the cylinder as a function of time, $\theta_{exp}(t)$, will be used in the following analysis to obtain a constant value for friction moment in the hinge.

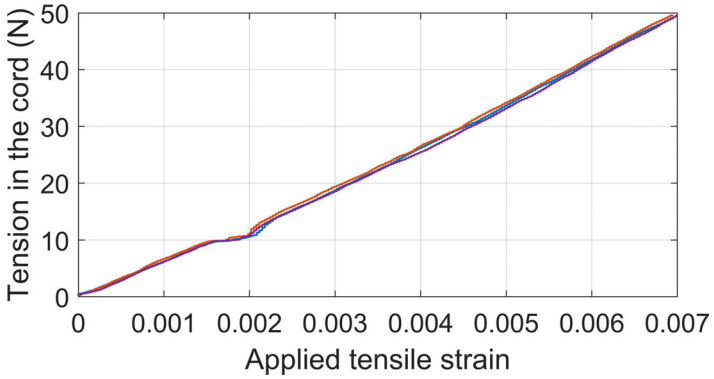

Fig. 7 Response of the cord to applied tensile strain. Measurements from three repetitions of the tensile test are presented.

The equation of motion of the cylinder at a rotation angle θ is

$$Mgd\sin(\theta+\theta_0)+T_e-T_f=I_h\ddot{\theta}, \tag{2}$$

with the initial conditions

$$\theta(0)=0 \quad \text{and} \quad \dot{\theta}=0, \tag{3}$$

where M is the measured mass of the cylinder, g is the acceleration due to gravity, T_e is the elastic moment due to the torsion spring in the hinge, T_f is the opposing friction moment, I_h is the rotational moment of inertia about the hinge axis, d is the distance of the center of gravity from the hinge axis, θ_0 is the angular position of center of gravity from the hinge axis with respect to the longer edge of the cylinder.

The hinge has two torsion springs with measured stiffness of 54.1 Nmm/rad each. Since each spring was pre-compressed by 180^o, the elastic moment is given by

$$T_e=108.2(\pi-\theta)\ \text{Nmm}. \tag{4}$$

The location of the center of gravity of the cylinder was obtained from the CAD model and was verified with experiments. Moment of inertia I_h was obtained from the CAD model.

The equation of motion 2 has two unknowns, constant T_f and $\theta(t)$, and needs to be solved iteratively. For a given value of friction moment T_f, Equation 2 can be integrated numerically to obtain the rotation as a function of time, $\theta_{an}(t)$. The value of T_f that minimizes the difference between the experimental measurement and the analytical result,

$$J=\text{norm}\left(\theta_{exp}-\theta_{an}\right), \tag{5}$$

was searched for using the unconstrained optimization solver `fminunc` in MATLAB.

The aforementioned experiment was repeated four times and four corresponding values for friction moment were obtained. The average value $T_f=137.9$ Nmm was used in the numerical simulations that follow.

D. Coefficient of friction of the pulleys

Deployment of the cord ends is driven by gravity. The deploying force is carried by the cords which go over pulleys. Due to friction in the pulleys, the tension force available to deploy the structure is smaller than the force applied at the loose end of a cord.

The miniature pulleys made of acrylic are mounted over ball bearings. We aim to approximate the friction moment in this assembly as a linear function of the total radial force acting on it. This linear behavior will then be simulated using *hinge* connector element in Abaqus [7].

The experimental setup consists of two identical pulleys at the same horizontal level (Figure 9). The cord (of the same material used in the deployment experiments) running over the two pulleys is connected to two masses. When released, the heavier mass moves downward and the lighter mass upward. The reflective spheres attached to two masses were tracked using OptiTrack motion capture cameras at a speed of 200 fps.

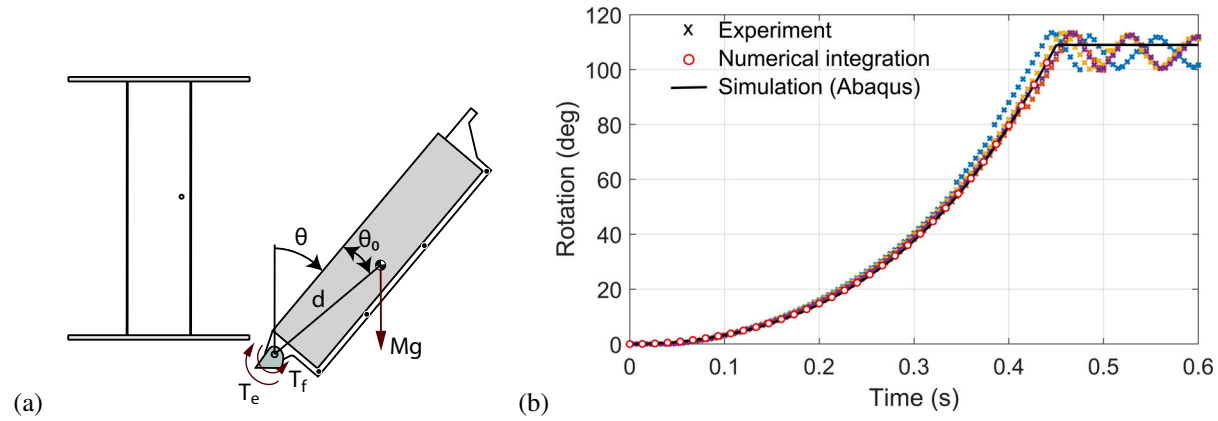

Fig. 8 (a) Schematic of the deploying cylinder in the absence of the structure. (b) Rotation of the cylinder with time. Friction moment T_f = 137.9 Nmm was used for the curves from numerical integration and Abaqus simulation. Cylinder locks at a rotation of 109^o in the simulation.

Applying Newton's second law of motion at masses M_1 and M_2,

$$T_1 = M_1(g + \ddot{h}), \tag{6}$$

$$T_2 = M_2(g - \ddot{h}), \tag{7}$$

where T_1 and T_2 are the tension forces in the cord at M_1 and M_2, respectively, g is the acceleration due to gravity, and $\ddot{h}$ is the acceleration of the masses.

The equations of rotational motion of the two pulleys are

$$TR - T_1R - M_{f1} = I\ddot{\beta}, \tag{8}$$

$$T_2R - TR - M_{f2} = I\ddot{\beta}, \tag{9}$$

where T is the tension in the portion of the cord between the two pulleys, R and I are the radius and moment of inertia of the pulleys, respectively, M_{f1} and M_{f2} are the friction moments in the left and right pulleys, respectively. When there is no slip between the cord and a pulley, rotation $\beta = h/R$.

The vertical displacement h of the masses we measured is a quadratic function of time, so the acceleration $\ddot{h}$ is a constant and is known. Therefore, tension forces T_1 and T_2 in Equation 6 are known. The moment of inertia I was previously measured in [**?**] to be 1.9×10^{-8} kgm^2. To solve the three unknowns T, M_{f1}, and M_{f2} in Equation 8, we used the optimization solver `fmincon` in MATLAB.

Assuming that the friction moment in a pulley is directly proportional to the total radial force at the pulley bearing,

$$M_{f1} = \mu_1 r F_{n1}, \tag{10}$$

$$M_{f2} = \mu_2 r F_{n2}, \tag{11}$$

where μ_1 and μ_2 are the coefficients of friction in the pulleys, r = 1.59 mm is the radius of the bore, and F_{n1} and F_{n2} are the total reaction forces at the pulleys.

The force resultants on the pulleys are

$$F_{n1} = \sqrt{T_1^2 + T^2}, \tag{12}$$

$$F_{n2} = \sqrt{T_2^2 + T^2}. \tag{13}$$

This experiment was conducted with 21 different combinations of masses (Figure 10) with 2 to 4 repetitions for each combination. Using linear fits, the coefficients of friction were found to be 0.0323 and 0.0326 for the two pulleys.

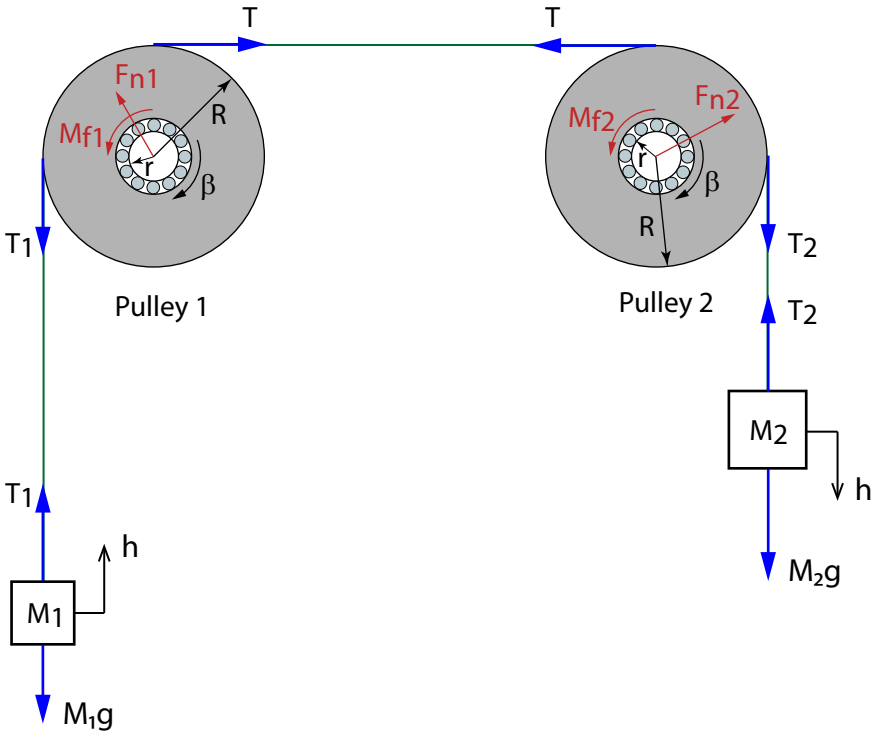

Fig. 9 Schematic of the experiment to measure the friction coefficients of the pulleys.

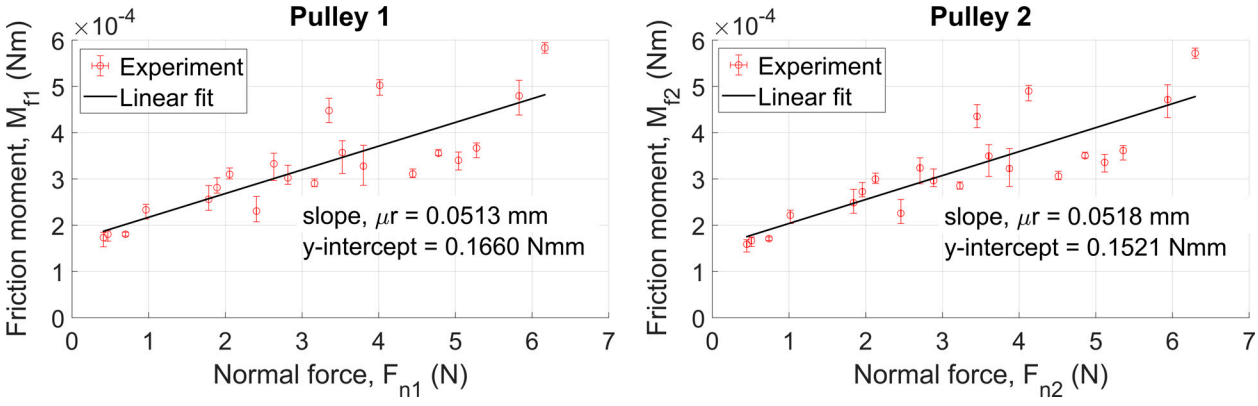

Fig. 10 Friction moments in the pulleys in relation to the total radial forces acting at the centers. In pulley 1, coefficient of friction, $\mu_1 = 0.0322$, and in pulley 2, $\mu_2 = 0.0326$. The mean value $\overline{\mu} = 0.0324$ is used in the finite element analyses.

IV. Numerical simulations

Using the data presented in Section III for the composite laminates and the components of the deployment mechanism, we implemented explicit dynamic simulations in the commercial finite element package Abaqus, version 2020.

To simulate the deployment of the structure, the initial condition is its folded configuration at rest (zero kinetic energy) which is unknown. Therefore, a first, key step of the analysis is to determine the folded configuration, starting from the known geometry of the unfolded structure. The exact path taken to achieve the folded configuration is unimportant as long as the total energy is conserved and the kinetic energy is negligible at the end of the folding process. The procedure used to simulate the folding process in this study was as follows.

1) We began the analysis with a Z-folded structure with all the longerons, battens, and cords in their unstressed states (Figure 11).
2) To induce elastic folds in the TRAC longerons, the flanges were flattened by pinching the longerons. To pinch a longeron, a small pressure normal to the surface of each flange was applied over a length of 25 mm in the middle of the longeron.
3) All the longerons were then folded by applying vertical displacements to the ends of the suspension cords (regions of the cords between pulleys and hanging masses) as shown in Figure 11. During this, the tensions in the suspension cords were linearly ramped up to their intended value F or when hanging masses were used to drive deployment, gravity was linearly ramped up to its final value.
4) The displacement boundary conditions at the tips of the suspension cords were released and the structure was allowed to reach its natural folded state under the influence of the applied deploying forces. During this process, viscous damping pressure was applied over all the surfaces to dissipate the kinetic energy. It was linearly ramped up to its intended value, held constant for a certain duration, and linearly ramped back to zero.

The rigid components of the mechanism such as the semi-annular plate and the cylinder were modeled using quadrilateral shell elements R3D4. The mesh size for the cylinder was 2 mm. Interactions between surface pairs surfaces was modeled as frictionless, hard contact.

A. Modeling the deploying cylinder

The pre-compressed, elastic torsion spring used to deploy the cylinder and the constant friction moment in the hinge were modeled in Abaqus using the connector element `hinge`. In the folded state, the rotation of the hinge connector about its axis was set equal to zero. This rotation constraint was deactivated at the beginning of the deployment step. The dynamics of the cylinder deployment, without the structure, was found to agree with that in experiments (Figure 8).

B. Modeling the strips

The composite laminates were modeled using quadrilateral shell elements with reduced integration, S4R. The flange and web sections of the longerons were modeled individually with the generalized stiffness values listed in Table 2. The mesh size for these elements was 3 mm.

The battens were modeled as isotropic beams with Young's modulus of 137 GPa and Poisson ratio 0.3. Beam elements B31 each of length 4 mm were used for the finite element discretization.

The rigid connections between battens and the corresponding longeron were modeled using kinematic couplings. The end of a batten was rigidly coupled to the nodes over a small region of the corresponding web laminate. This means that every degree of freedom was constrained to be equal at all the nodes involved in the coupling.

With the mentioned finite element mesh sizes, the stable time increment in the explicit analysis was approximately 7.4×10^{-8} s, and the critical elements deciding this time increment are the beam elements used to model the battens. To increase the stable increment of the analysis—to reduce the overall computation cost—a mass scaling can be applied to artificially raise the material density of a batten. However, it was observed that the deployment dynamics of the structure are highly sensitive to the mass of the structure. Therefore, no mass scaling was applied in any step of the analysis.

C. Modeling the cords

As mentioned earlier, each of the two cords is fixed at one end to the central shaft, goes through six strip-cord connectors, goes over a pulley, and is connected to a force or a hanging weight (as in our experiment) at the other end. In the simulations, the cords were modeled with `slipring` connector elements. The elastic behavior observed in Figure 7 was provided as an input to these elements. A slipring element in Abaqus is defined as a straight line between two nodes. Each node has a *material flow* degree of freedom in addition to three translations. This degree of freedom allows the

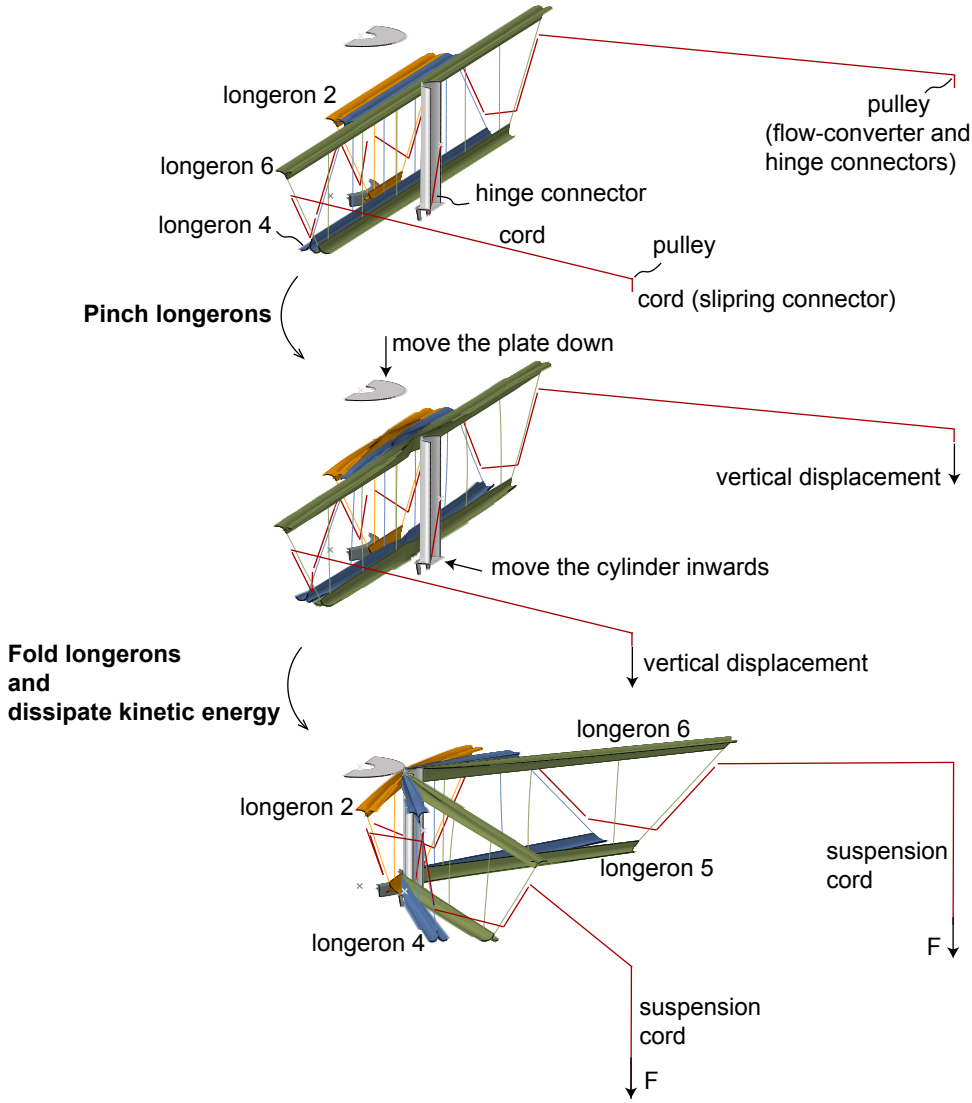

Fig. 11 Illustration of the steps to achieve a folded configuration in the finite element simulations.

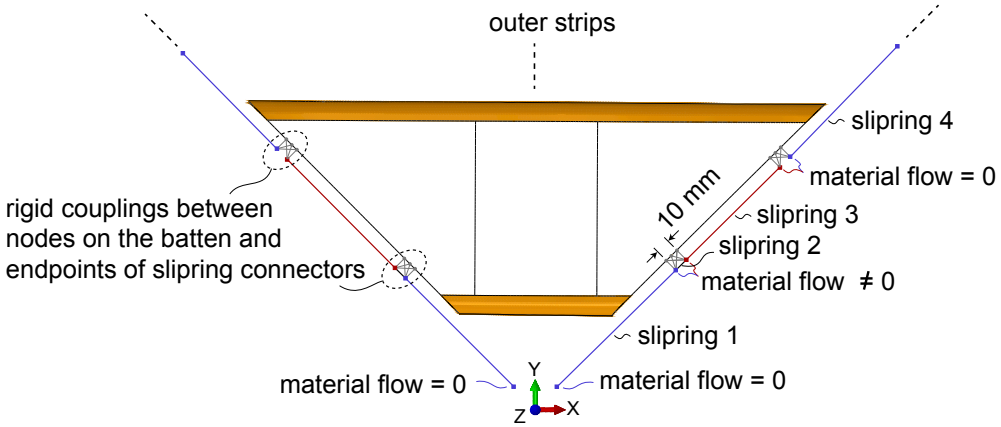

Fig. 12 Cords were modeled using slipring connector elements in Abaqus.

flow of material between two adjacent elements (or portions of a cord). Where the end of a cord is rigidly bonded to a batten or to the central shaft (Section II.A), material flow was constrained to be zero (Figure 12).

To simulate a rigid strip-cord connector of finite width, two nodes were placed at a distance of 10 mm and were rigidly coupled (constraining all six degrees of freedom) to the nodes over the same span of the batten (Figure 12). These two nodes represent the two sides of the strip-cord connector that the cord goes through.

D. Modeling the pulleys

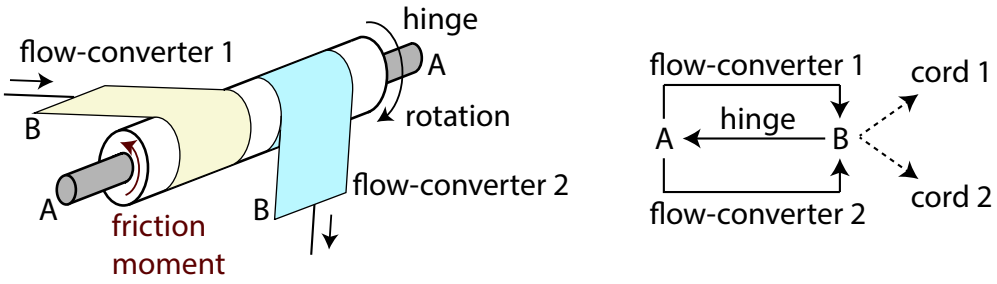

Fig. 13 Modeling a pulley using flow-converter and hinge connector elements in Abaqus. Nodes A and B are coincident. Two segments of the cord are connected at node B.

Abaqus allows flow of material between two adjacent slipring elements at their common node. Such a joint is, by default, frictionless and a special arrangement was needed to model the friction moment in the pulleys (as described in Section III.D).

The connector element `hinge` can model friction between two rotating surfaces. Specifically, the friction moment at the interface, about the axis of rotation, can be made to linearly vary with the total reaction force (see Figure 9 and Equation 10). To convert the material flow of the cord at one side into rotation of the hinge, and to convert the same rotation into material flow at the other side, two `flow-converter` elements were used. This conversion emulates a no-slip contact between the cord and the pulley. These three elements were defined between coincident nodes A and B as shown in Figure 13. The specific ordering of the nodes within a connector element and the boundary conditions at the nodes was chosen based on the definition of these elements in Abaqus. The translation degrees of freedom at node A, and the rotation degrees of freedom at node B were set to zero. The two slipring elements modeling the two segments of the cord on either side of the pulley are connected at node B.

V. Results

A. Explanation of the folded configuration

The folded configuration of the structure, prior to deployment, is shown in Figure 14. For a qualitative comparison, a top view of the folded structure from an experiment is provided. At a first glance, our simulations capture the folded configuration accurately. Quantitative comparisons are provided in the following sections.

The two cords holding the three strips together transmit the force that causes the deployment. Each cord is rigidly bonded to the strips at the outermost strip-cord connectors of every strip (shown in black in Figure 14. This is done to ensure that the required length of the cord is available between a pair of strips to make the deployment possible. The required cord length is the length of the cord between the pair of strips in the fully deployed state (Figure 2).

The forces that cause deployment act directly upon the outermost strip-cord connectors C16 and C26 and are not transferred to the interior segments of the cords. Due to the elastic strain energy stored in the folded strips, a certain amount of force is required to prevent them from unfolding. This required force results from the tension forces in the interior segments of the cords. Therefore, the folded configuration of the interior strips (Strips 1 and 2) is dictated by the lengths of the cords between strips.

A longeron is said to have latched when it snaps back into its unfolded state i.e. when the fold angle first becomes approximately 180^o. The longerons (1 and 2) of the innermost Strip 1 are the least folded and are very close to their latched state. Hence the tension force required to keep the strip folded is very small compared to the applied force. When deployed, these longerons move almost straight along the $y-$ axis while the strip rotates about the $x-$ axis to

reach its deployed state (Figure 15). The longerons (5 and 6) of the outermost Strip 3 are the most folded and follow more complex paths to reach their latched state. Upon deployment, the structure exhibits highly transient oscillations as seen at the end of every curve in Figure 15. While in experiments these oscillations are naturally dissipated and the structure comes to complete rest, the structure in the simulation continues to oscillate.

B. Experiment vs simulation

To compare the implemented numerical simulations with the experiments, we performed the deployment of the structure with two different hanging masses: 300 gram and 400 gram. Reflective markers on the structure were tracked using the infrared motion capture cameras mentioned in Section II.C.

The outermost strip-cord connectors C16 and C26 are directly driven by the hanging masses and their motion should be the easiest to predict, followed by the motion of the interior connectors. As an example, a comparison of the Cartesian coordinates of three strip-cord connectors is shown in Figure 16.

It can be seen that the initial positions (at 0 s) of the connectors in simulation are in excellent agreement with the experiment. Our simulations estimate the motion of C26 with good accuracy until approximately 0.4 s of deployment i.e., until the time when the hanging weights reach the bottom of their motion range. At this time, the tension forces in the suspension cords rise significantly for a short time duration to oppose the momentum of the weights. After this time, the x and y coordinates are estimated with better agreement with experiments than the vertical z coordinates.

The least agreement with the experiment is found for the innermost strip-cord connector C22 (Figure 15). However, the deployment parameters of concern in this study—time to latch and extreme heights of the structure—are dictated primarily by the outer strips (Strips 2 and 3 in Figure 2), and we consider this small disagreement with the experiment acceptable.

Going a step further in the verifying the simulations, we compare the fold angles in all the longerons (Figure 17). It was observed in the experiments and simulations that the elastic folds remain in the middle of the longerons for most of the deployment. Hence, two markers (in experiment) or two nodes (in simulation) at the longeron-batten intersections on either side of the middle of a longeron are used to define the fold angle. The two vectors connecting these two pairs of markers or nodes define the fold angle. In the few instances where the fold is not in the middle of a longeron or where there are multiple folds, the angle between the two vectors does not represent the true fold angle. However, the comparison is still valid since the parameter being compared is the same in both experiment and simulation.

At a first glance, the time histories of the fold angles from the simulations and experiments appear to be the same. The amount of agreement between the two decreases at approximately 0.4 s of deployment, when the hanging weights reach their minimum vertical positions undergoing an impact. The initial fold angles (at 0 s) and initial dynamics in simulation agree reasonably well with the experiments in the case of 300 g masses, and agree quite accurately in the case of 400 g masses.

Initial trends (until 0.4 s of deployment) of the fold angles in Strip 3 look similar in both test cases while those for the interior strips vary significantly. This is because the outermost strip is driven directly by the hanging masses and the two different masses seem to have nearly the same effect on the deployment as explained below.

The deployment time is defined as the time taken for all the longerons to first latch into their deployed configuration. The deployment times for the two test cases are listed in Table 3 and differ by approximately 10%.

Although we expected that the deployment would be faster when hanging masses are increased, the results show practically no change. Although the initial dynamics of the deployment are different with different hanging masses, the time taken for all the longerons to latch into their unfolded state is almost identical. The key factor affecting this behavior is the effective deploying force i.e. the tension in the suspension cord. Due to the inertia of the hanging masses, the tensions in the suspension cords are of comparable magnitudes and have similar time histories (Figure 18).

Table 3 Simulation vs. experiment: comparison of deployment times.

Hanging masses	Simulation	Experiment
300 g	0.503 s	0.56 s
400 g	0.508 s	0.56 s

C. Constant-force deployment

With the fidelity of the numerical simulations established, we can study a variety of deployment schemes. We begin by studying the dynamic deployment of the structure driven by constant forces in the suspension cords. This emulates the practical choice of using constant-force spring retractors to drive the deployment.

We noticed that the friction in the pulleys can significantly affect the deployment dynamics. The friction moment in the pulleys was modeled only to verify the simulations against experiments, and is not a quantity of inherent interest as the pulleys should ideally be eliminated in future deployment system designs. Therefore, the simulations discussed hereafter do not use pulleys. We performed two additional finite element simulations of deployment, one with gravity enabled and the other with gravity disabled. To be able to compare these test cases with the hanging-mass-driven deployment presented earlier (Section V.B), the applied deploying force in the suspension cords is chosen to be equal to the weight of a mass of 300 gram i.e., $F = 2.942$ N, and is held constant throughout the deployment.

In the absence of gravity, the maximum height the structure reached is approximately 100 mm greater than the maximum height it reached when gravity was enabled. However the shapes of the deployment envelope looked similar in both cases (not presented here). In addition, the deployment time with or without gravity is the same (Table 4). Therefore, it can be concluded that deployment tests in the presence of gravity data can be used to gain a good insight into in-space deployment of these structures.

D. Effect of the cylinder

As discussed earlier, the deployment mechanism uses a cylinder to hold the structure in its folded configuration. When released, the cylinder rotates about the hinge axis and takes a finite time to reach its rotated configuration. The structure remains in contact with the cylinder for more than half the time taken for full deployment. It appears that the cylinder acts as a ramp causing the structure to reach higher vertical positions. To verify this, we simulated an imaginary (yet easy to implement in reality) situation where the cylinder clears the structure instantly upon release. In other words, the deployment happens 'without a cylinder'.

The maximum and minimum heights the structure reaches during the deployment with and without the deploying cylinder are presented in Figure 19. Vertical ($z-$) positions of the nodes along the edges of the webs of all the six TRAC longerons were considered in this search. The deployment progress is defined using the mean radial distance traveled by the outermost strip-cord connectors C16 and C26. Deployment progress is 100% when the mean radial distance of the connectors reaches its maximum. For deployment with a cylinder, this maximum occurs at 0.4 s, and without a cylinder, it occurs at 0.12 s.

When a cylinder is used, the maximum height of the structure starts to increase at approximately 0.15 s. This rise in the slope happens once the outermost longeron (6) clears the deploying cylinder. Longeron 6 is the closest to the outermost strip-cord connectors, that are directly driven by the deploying forces. Once this longeron loses contact with the deploying cylinder, the outermost strip (3) starts to ramp up while rotating as seen in Figure 21. In the absence of the cylinder, Strip 3 rotates in a similar fashion but without reaching the same heights. Also, the deployment happens much sooner (Table 4) and is smoother (Figures 19 and 20).

When the deployment is not hindered by the presence of the cylinder, the structure reaches its maximum height at 0.17 s while the outermost strip-cord connectors already reached their maximum radial distance at 0.12 s. This means that the structure reaches its maximum height while Strip 3 rotates after reaching its maximum radial distance (see Figure 21). On the contrary, when the cylinder is present, the structure reaches its maximum height at 0.33 s before the outermost connectors reach their maximum radial distance at 0.4 s.

At 50% of deployment without a cylinder, the vertical displacement of the highest points on the structure is 61mm while for the deployment with a cylinder, it is 216 mm. Also, within the first half of the deployment, the vertical displacement of the lowest points is only 39.2 mm (downward) without the cylinder, as compared to 71.4 mm (downward) with the cylinder. Therefore, the structure safely clears any obstacles at the center of the deployment mechanism when the cylinder instantaneously clears the structure

Table 4 Time taken for deployment in simulations with constant deploying force F = 2.942 N.

Deploying cylinder	Gravity	Deployment time
ON	ON	0.605 s
ON	OFF	0.603 s
OFF	OFF	0.406 s

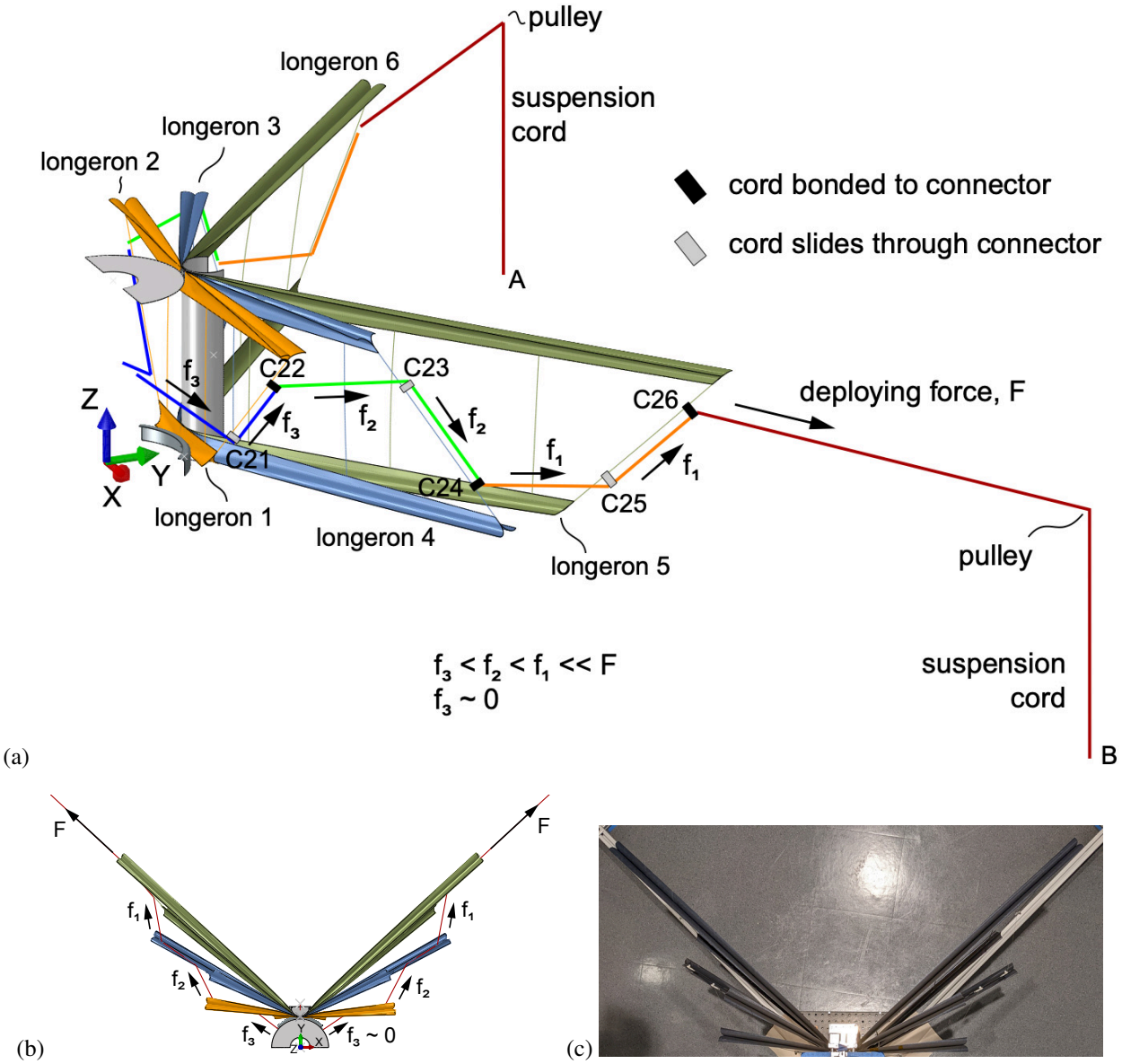

Fig. 14 Structure in folded state: (a) perspective view and (b) top view in simulation, and (c) top view in an experiment. Cord is rigidly bonded to alternate strip-cord connectors hence the discontinuity in tension forces. Deploying force acts directly on the outermost strip. Fold angles in the inner strips are determined only by the unextended lengths of the cords. The innermost cords attached to the central shaft are slack.

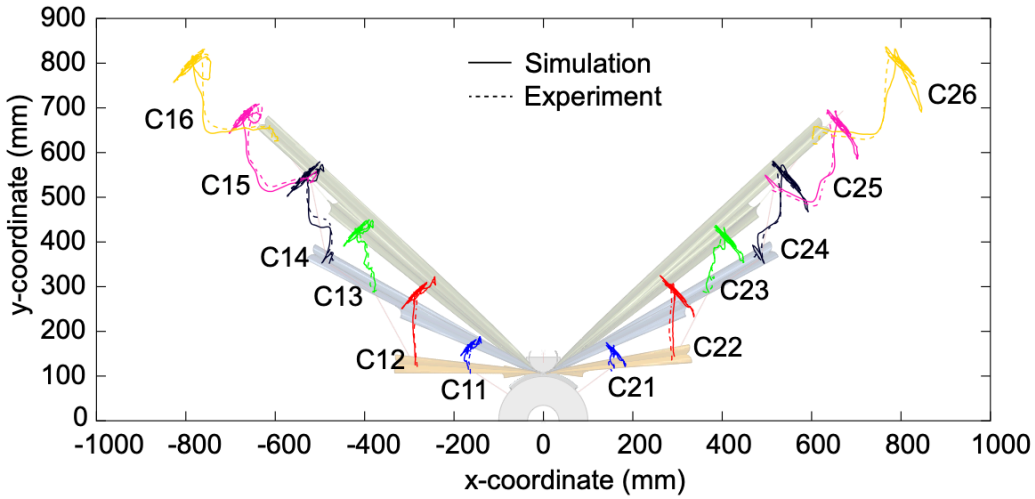

Fig. 15 Simulation vs. experiment: comparison of the x and y coordinates of the strip-cord connectors during the first 1 s of deployment. The hanging masses are 300 g. A top view of the folded structure is included in the background to assist the visualization.

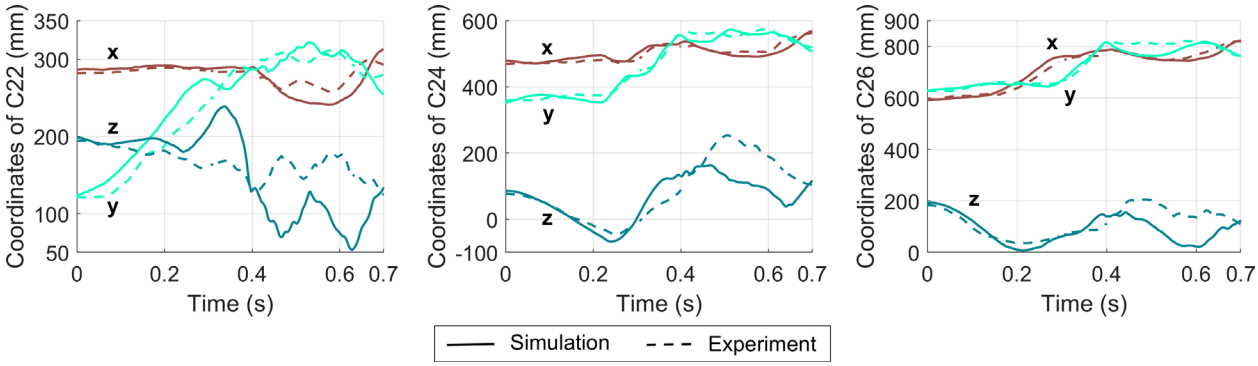

Fig. 16 Simulation vs. experiment: comparison of the spatial coordinates of the strip-cord connectors C22, C24, and C26. The hanging mass are 300 g.

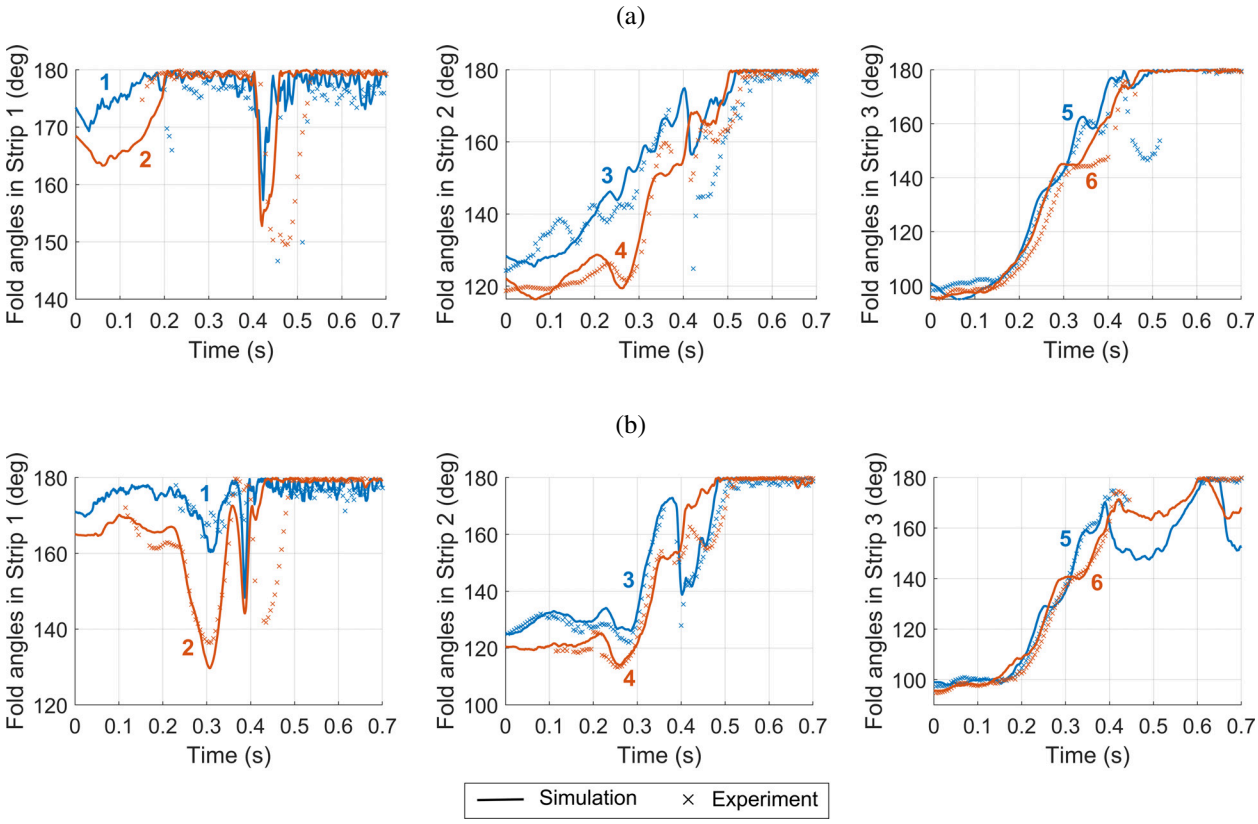

Fig. 17 Simulation vs. experiment: comparison of the fold angles in the longerons. Longeron IDs as defined in Figure 2 are marked against the corresponding curves. Hanging masses are 300 g in (a), and 400 g in (b).

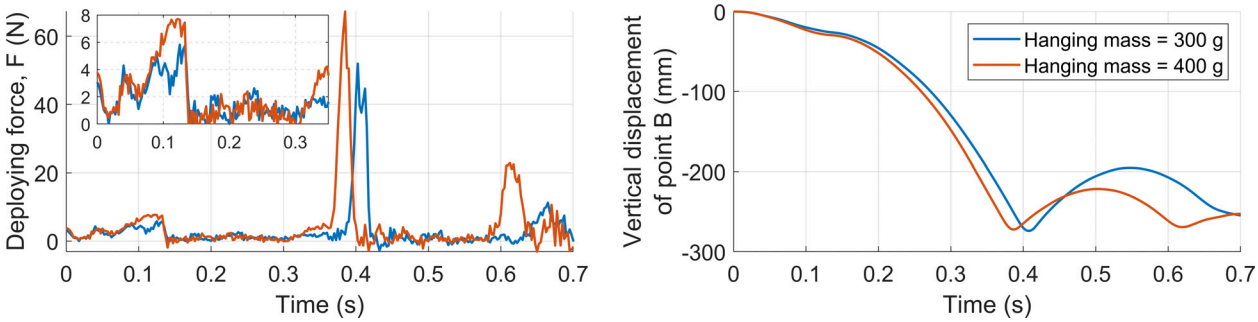

Fig. 18 Effective deploying force in the suspension cord and vertical displacement of the hanging mass at point B. Tension in the cord rises suddenly at approximately 0.4 s to absorb the momentum of the hanging mass.

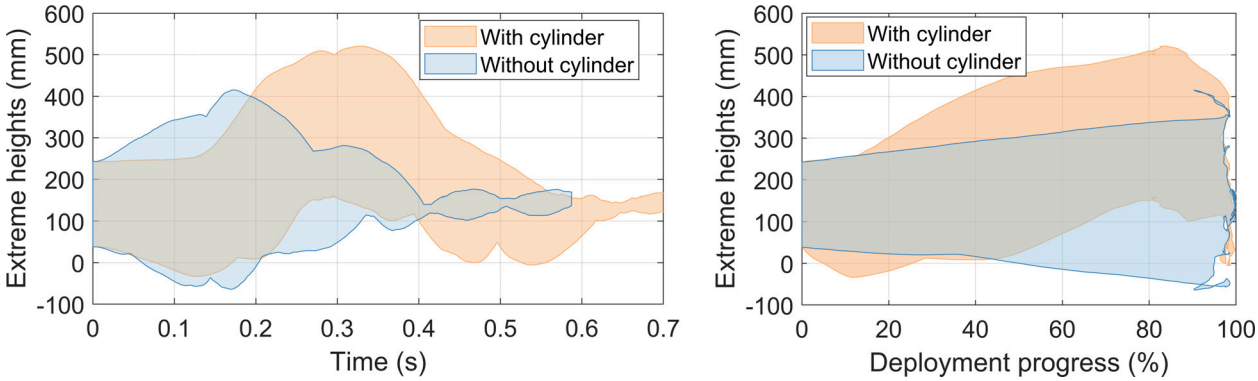

Fig. 19 Maximum and minimum heights reached by the structure during deployment with and without the cylinder. Gravity is absent and the deploying force $F = 2.942$ N in both cases.

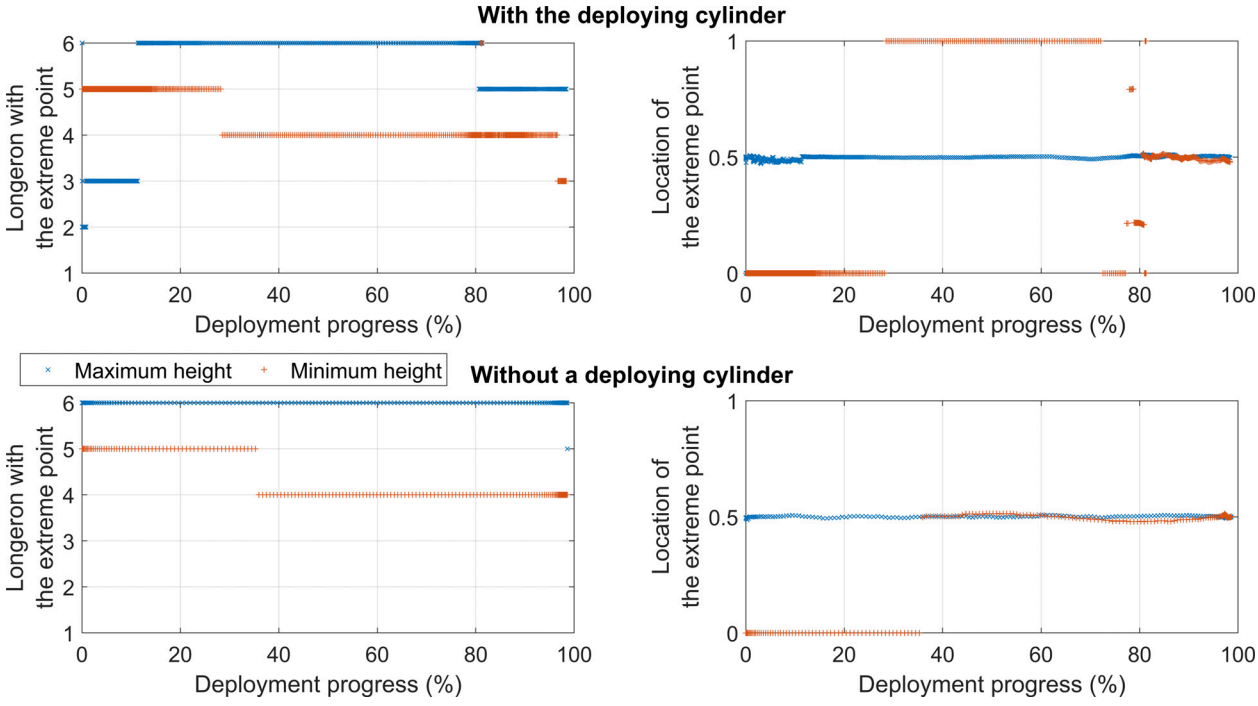

Fig. 20 (Left) Longerons containing the nodes at maximum and minimum heights at a given instant. Longeron IDs are as defined in Figure 2. (Right) Relative positions of these nodes along the lengths of the longerons containing them. Without the cylinder, the middle of the outermost Longeron 6 is at the maximum height at any instant.

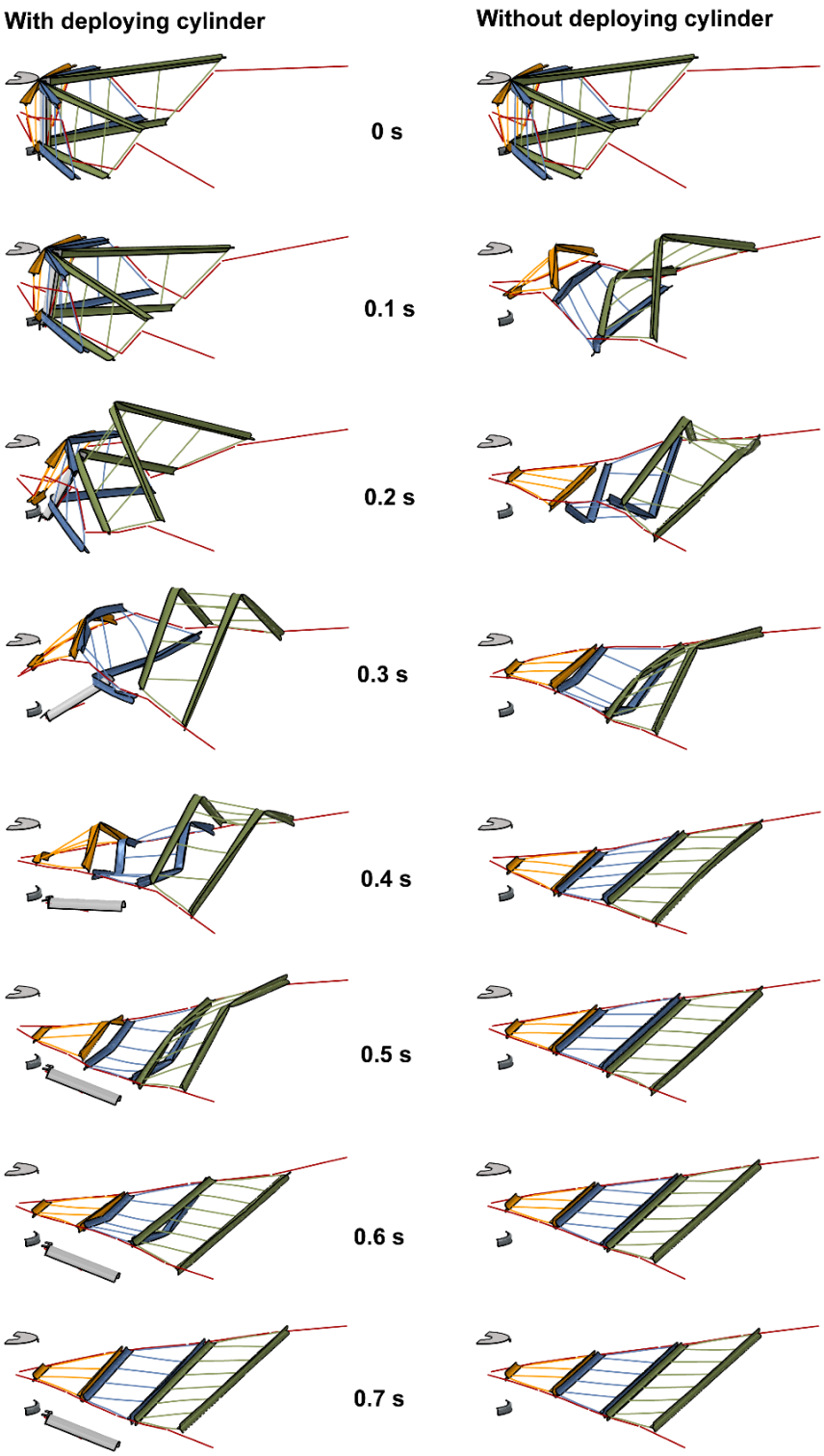

Fig. 21 Deformed profiles of the structure deploying with the cylinder (left) and without the cylinder (right). In both cases, gravity is absent and the constant deploying force is 2.942 N.

VI. Conclusions

Unconstrained dynamic deployment of the ultralight deployable space structures developed by the Caltech Space Solar Power Project (SSPP) was studied using experiments and numerical simulations. For the purpose of verifying the numerical simulations, deployment tests of the structure triggered by hanging weights were conducted, and the motion of the structure was tracked using motion capture cameras. The simulations developed in the commercial finite element package Abaqus show good agreement with the experiments. The simulation procedure developed in this study can be utilized to study a wider range of thin shell deployable structures, beyond this Caltech project. The deployment of the structure triggered by constant forces in the cords, in the presence and absence of gravity was simulated. The results show that the deployment tests in the presence of gravity data can be used to gain a good insight into in-space deployment of these structures. The effect of the cylinder on the deployment dynamics was studied by simulating the deployment without a cylinder. It was shown that the deployment envelope without the cylinder is significantly smaller and the structure would safely clear any obstacles at the center of the deployment mechanism. Hence, it is recommended that the Caltech SSPP deployment system avoid using rotating cylinders in the deployment mechanism. Outcomes of this research will not only benefit the Caltech project but will also contribute to the design of future lightweight deployable space structures that undergo unconstrained dynamic deployment.

Acknowledgments

This research was funded by the Space Solar Power Project at Caltech.
The authors thank Dr. Terry Gdoutos and Alan Truong for their help with CAD modeling and building the test structure; Noel Esparza-Duan, Michael O'Connell, Dr. Guanya Shi, Uba K. Ubamanayu, and George Popov for their help with motion capture experiments; and Dr. Antonio Pedivellano for advice on simulation models.

References

[1] Roybal, F., Banik, J., and Murphey, T., "Development of an elastically deployable boom for tensioned planar structures," *In 48th AIAA/ASME/ASCE/AHS/ASC Structures, Structural Dynamics, and Materials Conference,* 2007, pp. 1838.

[2] Murphey, T. W. and Banik, J., "Triangular Rollable And Collapsible Boom," U.S. Patent 7895795 B1, filed on 22 October 2007 and published on 1 March 2011.

[3] Leclerc, C. and Pellegrino, S., "Nonlinear elastic buckling of ultra-thin coilable booms," *International Journal of Solids and Structures,* Vol. 203, 2020, pp. 46–56.

[4] Pedivellano, A. and Pellegrino, S., "Deployment Dynamics of Thin-Shell Space Structures," *Journal of Spacecraft and Rockets,* 2022, Vol. 59(4), pp. 1-14.

[5] Gdoutos, E., Sommer, C.F., Truong, A., Wen, A., Pedivellano, A., Ubamanyu, K., Madonna, R.G. and Pellegrino, S., "Development of the Deployable on-Orbit ultraLight Composite Experiment (DOLCE) for the Space Solar Power Project Demonstration Mission," *In AIAA SCITECH 2022 Forum,* 2022, pp. 1266. https://doi.org/10.2514/6.2022-1266, URL https://arc.aiaa.org/doi/abs/10.2514/6.2022-1266.

[6] Daniel, I. M., Ishai, O., "Engineering mechanics of composite materials," New York: Oxford university press, 2005.

[7] Smith, Michael., "ABAQUS/Standard User's Manual," Version 6.9. Providence, RI : Dassault Systèmes Simulia Corp, 2009.